



A Control-Free Series Resonant Converter for Battery Charging With Automatic CC-to-CV Profile and Whole-Process High Efficiency

Zhijian Fang , Member, IEEE, Haojiang Yue, Student Member, IEEE, Zihao Wei, Student Member, IEEE, Zihan Zhang, Student Member, IEEE, and Zhicong Huang , Member, IEEE

Abstract—Constant current (CC) and constant voltage (CV) outputs are required by electric vehicle chargers to comply with the battery profile, which are challenges to the wide operating range, accurate current and voltage control, and high efficiency of the battery chargers. This article proposes a control-free battery charger based on a series resonant converter that features an inherent automatic CC-to-CV profile and whole-process high efficiency. Both the CC and CV modes enjoy identical switching sequences and operating waveforms, and the transition of CC-to-CV depends on the load condition. Automatic and smooth CC-to-CV transition can also be obtained after the CC charging process, thus avoiding the overvoltage charging risk. Detection of battery state and active control for the charging profile can, therefore, be eliminated, making the proposed battery charger rugged and reliable. The CC and CV outputs are flexibly configurable by setting the operating frequency and designing the turn ratio of the transformer, respectively. Moreover, with an assistive circuit, soft switching can be realized for all switches regardless of the operating conditions to achieve a high efficiency throughout the whole charging process. Finally, a 1-kVA prototype is presented to validate the control-free and automatic CC-to-CV profile. High efficiency up to 98.4% is measured during the whole CC and CV charging periods.

Index Terms—Battery charging, constant current (CC), constant voltage (CV), high efficiency, series resonant converter (SRC), soft switching.

NOMENCLATURE

ω_r	Resonant angular frequency.
A_e	Cross-sectional area of the core.
B	Magnetic flux density.
B_m	Maximum magnetic flux density.

Manuscript received 26 November 2022; revised 9 March 2023; accepted 12 April 2023. Date of publication 21 April 2023; date of current version 19 May 2023. This work was supported in part by the National Natural Science Foundation of China under Grants 51707138 and 52007067 and in part by the Natural Science Foundation of Guangdong Province under Grants 2022A1515011581 and 2023A1515011623. Recommended for publication by Associate Editor John Lam. (Corresponding author: Zhicong Huang.)

Zhijian Fang, Haojiang Yue, Zihao Wei, and Zihan Zhang are with the Hubei Key Laboratory of Advanced Control and Intelligent Automation for Complex Systems and the School of Automation, China University of Geosciences, Wuhan 430074, China (e-mail: fangjianhust@gmail.com; yuehaojiang@cug.edu.cn; weizihao@cug.edu.cn; zhan303@cug.edu.cn).

Zhicong Huang is with the Shien-Ming Wu School of Intelligent Engineering, South China University of Technology, Guangzhou 510006, China (e-mail: zhiconghuang@scut.edu.cn).

Color versions of one or more figures in this article are available at <https://doi.org/10.1109/TPEL.2023.3269044>.

Digital Object Identifier 10.1109/TPEL.2023.3269044

C'_p	Equal capacitance of series C_p and C_r .
C_{ds}	Drain–source capacitance of the switchers.
C_p	Parasitic capacitor.
C_r	Resonant capacitor.
$D_1 - D_4$	Secondary-side diodes.
f_r	Resonant frequency.
$f_{s,max}$	Maximum switching frequency.
f_s	Switching frequency.
i_{Di}	Current of diodes D_i .
i_{in}	Input current.
i_m	Magnetic current.
$I_{o,max}$	Maximum charging current.
i_{off}	Instantaneous current value at turn-OFF time.
I_o	Output current.
$I_{r,RMS}$	RMS value of resonant current.
i_r	Resonant current.
i_{Si}	Current of switches S_i .
i_{ssi}	Current of damping circuit S_{si} .
k, α, β	Constants of transformer determined by magnetic material.
L_m	Magnetic inductance.
L_r	Resonant inductance.
n	Turn ratio.
N_2	Transformer secondary turns.
p	Action number of each switcher during one switching period.
P_{OFF}	Switching loss.
$P_{sw.,cond.}$	Conduction loss of the switchers.
$P_{tr.,cond.}$	Transformer conduction loss.
$P_{tr.,core.}$	Transformer core loss.
R_d	Damping resistor.
$R_{L,cri}$	Critical load resistor.
R_L	Load resistor.
$r_{sw.}$	Switcher ON-resistor.
$r_{tr.}$	Winding resistor of the transformer.
$S_1 - S_4$	Primary-side switches.
S_{s1}, S_{s2}	Damping circuit switches.
t_{off}	Turning-OFF time.
T_r	Resonant period.
T_s	Switching period.
v_{ab}	Terminal voltages of the primary-side bridge.
$V_{bat,max}$	Maximum battery voltage.
V_{bat}	Battery voltage.

v_{cd}	Terminal voltages of the secondary-side bridge.
v_{Di}	Voltage of diodes D_i .
V_{ds}	Drain-source voltage value at turning-OFF time.
V_i	Input voltage.
v_{r0}	Resonant voltage value at $t = t_0$.
v_{r1}	Resonant voltage value at $t = T_r/2$.
v_{r2}	Resonant voltage value at $t = T_r$.
v_r	Voltage of resonant capacitor.
v_{Si}	Drain-to-source voltage of switches S_i .
v_{ssi}	Drain-to-source voltage of switches S_{si} .
V_T	Transformer core volume.
Z_r	Characteristic impedance.

I. INTRODUCTION

NOWADAYS, dc–dc converters for battery charging applications are attracting more and more attention with the developments of electric vehicles [1], [2], [3]. To comply with the battery charging profile, these converters should be controlled to regulate the required constant current (CC) and constant voltage (CV) outputs. However, the battery voltage rises from near zero to the maximum value during the CC charging period, while the battery current drops from the rated value to near zero during the CV charging period. Wide output voltage and current ranges are required for the dc–dc converters, as well as high efficiency. Meanwhile, accurate CC and CV control is also desired to tackle the overcharging risk.

An *LLC* resonant converter is the most popular dc–dc converter for battery charging due to its outstanding advantages of soft switching, high power density, and high efficiency [4], [5]. To adjust the wide output voltage and current ranges of battery charging, a wide switching frequency range is required for the *LLC* resonant converter, which results in large power loss and bulky inductor, capacitor, and transformer. Many design methodologies of the *LLC* resonant converter are presented to adapt to the wide voltage range [6], [7], [8]. However, the switching frequency range is still wide, worsening the efficiency and power density. Burst control [9], [10], pulswidth modulation [11], phase-shift modulation [12], and energy feedback control [13] are proposed to narrow the switching frequency range under the wide load conditions. Synchronous rectifier control [14], variable topology [15], and variable dc-link voltage control [16], [17] are published to extend the voltage gain range. However, additional devices are required in these methods, increasing the converter cost and power loss. Moreover, the transfer functions between the switching frequency and output voltage and current are nonlinear, resulting in accurate voltage and current control issues.

To address the accurate control issues, feedback control is used to regulate the switching frequency for the resonant converter [18]. But the simple proportional–integral controller fails to comply with the nonlinear power features. In [19], the resonant capacitor voltage is used to compensate for the nonlinear characteristics at the cost of additional voltage sensors. Fang et al. [20] build an inverse function of the nonlinear converter model to linearize the power transfer features. But the dynamic performance is still poor. In [21], an optimal trajectory tracking

method is presented to improve the settling time. However, these control methods are complex and lack robustness. Accurate mathematical models are required rising the realization difficulty in practices.

To simplify the control and optimize the efficiency, a control-free battery charger, which features voltage-independent current and current-independent voltage, is attracting more and more attention and has been widely researched for the wireless power transfer applications [22]. In [23], several compensation topologies are proposed to obtain CC or CV outputs with fixed switching frequency. The CC and CV modes can be transferred by hopping the switching frequency. In [24], the variable topology is presented to switch CC and CV modes by using the bidirectional switches. However, the mutual inductance between transmit and reception coils are used to acquire the CC and CV features in the above methods, which cannot be applied for wired battery charging converters with a tight coupling transformer. The parallel resonant converter is presented to achieve CC and CV outputs by optimally choosing the switching frequency [25]. But the outputs are still affected by the loads. In [26], an *LCL*–*T* resonant converter is proposed to achieve the CC feature with a fixed switching frequency and special design. Despite the output current being independent of the voltage, the output voltage is unlimited in this method. Further charging with CC could damage the battery when the battery's natural voltage limit is reached. To address this issue, an *LCL*–*T* resonant converter with clamp diodes is proposed in [27] achieving inherent CC and CV limit features. But large reactive current appears in this converter due to the *LCL* resonant tank. In [28], a novel dual full-bridge *LLC* resonant converter is presented with inherent CC and CV characteristics, as well as the excellent features of the *LLC* resonant converter. However, the added full-bridge converter increases the power loss and cost.

To address these issues of battery charging applications, this article proposes a control-free battery charger based on the series resonant converter (SRC) with inherent and automatic CC-to-CV profile and whole-process high efficiency, which perfectly complies with the battery charging requirements. The output current and voltage are only up to the switching frequency, and the input voltage is independent of the load, achieving control-free features. A wide operation range and minimum switching frequency variation can be obtained reducing the power loss and difficulty of control and design. Especially, an automatic transition from CC output to CV threshold can be enabled during the battery charging process avoiding the risk of overcharging. High robustness without battery state of charge (SOC) detection can be achieved. Moreover, a damping circuit is added in the SRC to reduce the oscillation and enable all switches to realize soft switching during the whole operating range. A zero phase angle between the input voltage and current is also obtained. High-efficiency and control-free features are achieved for the whole CC and CV charging periods, which nicely satisfy the requirements of battery charging.

Compared to the conventional method, three advantages can be achieved by the proposed method.

- 1) Both zero-current switching (ZCS) ON and OFF simultaneously are realized over a wide output range in the

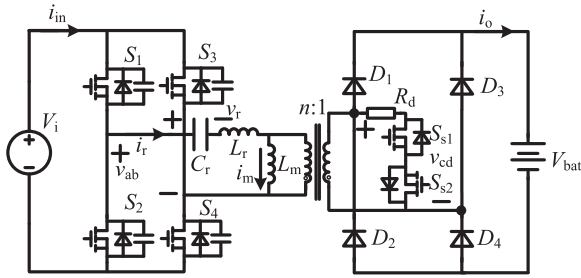


Fig. 1. Schematics of the proposed SRC.

proposed method, achieving a tiny switching loss for a wide range. In contrast, in the conventional method, only zero-voltage switching (ZVS) ON is realized suffering from hard OFF. Moreover, the ZVS feature could lose in light-load conditions resulting in large switching loss.

- 2) Second, a zero phase angle between the input voltage and current is obtained during the whole charging process in the proposed method, whereas large backflow current is needed in the conventional method to regulate the power, which results into large conduction loss.
- 3) Third, control-free and auto CC-to-CV profile can be achieved in the proposed method to enable high robustness without battery SOC detection. In the conventional method, a current controller and a voltage controller are needed in CC and CV charging periods, respectively. And a special detection strategy should be used to control the converter transit from CC to CV mode to avoid the overcharge risk.

The rest of this article is organized as follows. Section II details the proposed modulation scheme in CC and CV modes. The design considerations are presented in Section III. Section IV analyzes the power loss of the proposed converter. Experiments are conducted in Section V to validate the proposed modulation. Finally, Section VI concludes this article.

II. PROPOSED METHOD AND OPERATION ANALYSIS

The proposed topology is shown in Fig. 1, which includes a typical SRC and an assistive damping circuit. The damping circuit includes bidirectional switches (S_{s1} and S_{s2}) and a damping resistor (R_d) connected across the secondary side of the transformer. The SRC consists of a primary full-bridge circuit and a secondary full-bridge diode rectifier, interconnected with a series resonant tank (L_r - C_r) and a transformer.

The voltage and current waveforms for the SRC are presented in Fig. 2. Note that the modulation waveforms in CC and CV modes are the same, and thus, the transition of CC-to-CV is free of control. S_1 and S_4 are simultaneously turned ON at t_0 and keep ON for $T_r/2$ and T_r , respectively, where T_r is the resonant cycle. After S_1 is turned OFF, S_2 is ON for $T_r/2$. Then, S_1 - S_4 are all turned OFF and the assistive switches S_{s1} and S_{s2} are ON until the end of half-switching cycle $T_s/2$. The positive and negative half-switching cycles are dualities and, thus, not repeated.

Consequently, a square voltage v_{ab} waveform with a constant-time high-level state, zero-level state, and variable-time high-impedance state is generated to excite the resonant current,

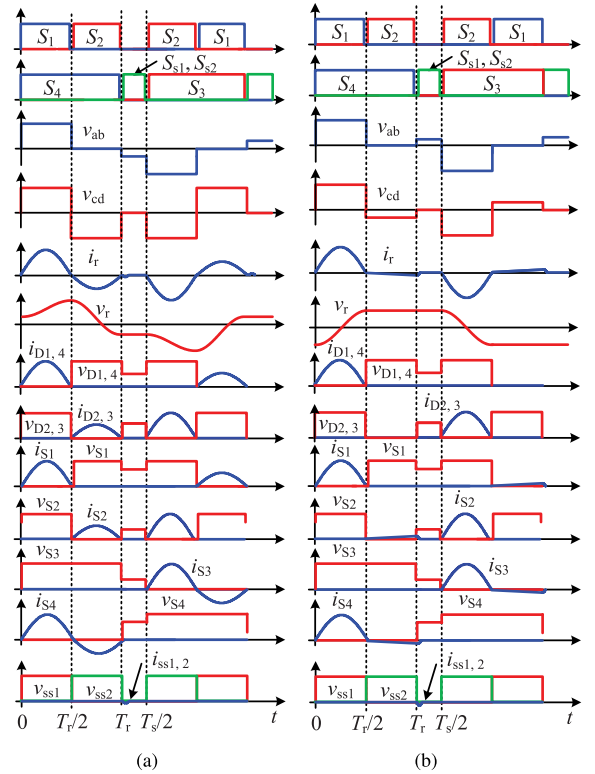


Fig. 2. Waveforms of resonant voltage and current with the proposed modulation. (a) CC mode. (b) CV mode.

whereas the voltage v_{cd} waveform is provided by the secondary rectifier, diodes D_1 - D_4 , the states of which are decided by the resonant current i_r . The operation mode of the proposed converter only depends on the load resistance. When the load resistance is small, diodes D_1 - D_4 are turned ON during 0 - T_r , and the converter works in the CC mode. Otherwise, the converter is in the CV mode. The detailed analysis is given in Sections II-A and II-B.

Noticeably again, the switching sequence and operating waveforms are identical for the CC and CV modes. The converter can autotransfer and smoothly transfer from the CC mode to the CV mode with the increase of load resistance.

A. CC Operation Mode

During the CC charging process, the battery voltage V_{bat} is low, providing small equal load resistances. The secondary rectifier is conducted during 0 - T_r , making the converter work in the CC mode. The resonant current and voltage waveforms are illustrated in Fig. 2(a). There are three stages in a half-switching cycle in the CC mode. Detailed descriptions are as follows.

1) *Stage 1* (t_0 - $T_r/2$): S_1 and S_4 turn ON during this period. $v_{ab} = V_i$, which is larger than nV_{bat} conducting the rectifier diodes D_1 and D_4 . V_i could charge nV_{bat} through resonant tank and transformer, as the circuit shown in Fig. 3(a). i_r and v_r can be written as

$$i_r = \frac{-v_{r0} + V_i - nV_{bat}}{Z_r} \sin(\omega_r t) \quad (1)$$

$$v_r = (v_{r0} - V_i + nV_{bat}) \cos(\omega_r t) + V_i - nV_{bat}. \quad (2)$$

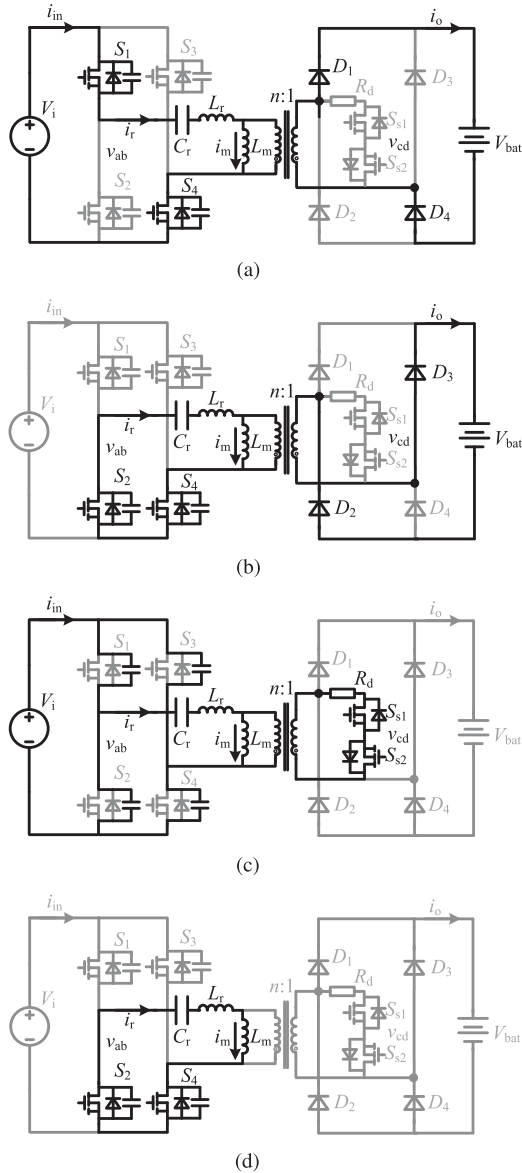


Fig. 3. Equivalent circuits of switching stage in the proposed method. (a) Equal circuit A. (b) Equal circuit B. (c) Equal circuit C. (d) Equal circuit D.

Z_r and ω_r are characteristic impedance and resonant angle frequency, respectively, defined by

$$Z_r = \sqrt{\frac{L_r}{C_r}}, \text{ and } \omega_r = \frac{1}{\sqrt{L_r C_r}}. \quad (3)$$

2) *Stage 2* ($T_r/2 - T_r$): After the half-resonant cycle, i_r reaches zero again. S_1 turns OFF, while S_2 turns ON realizing ZCS ON and OFF. Due to the low battery voltage V_{bat} , D_2 and D_3 could conduct during this period, despite $v_{ab} = 0$. The resonant tank continuously charges the battery, as the circuit shown in Fig. 3(b). i_r and v_r can be expected by

$$i_r = \frac{-v_{r1} + nV_{bat}}{Z_r} \sin[\omega_r(t - T_r/2)] \quad (4)$$

$$v_r = (v_{r1} - nV_{bat}) \cos[\omega_r(t - T_r/2)] + nV_{bat}. \quad (5)$$

3) *Stage 3* ($T_r - T_s/2$): After one resonant cycle, all switches turn OFF except S_{s1} and S_{s2} , which shorten the transformer, as the circuit shown in Fig. 3(c).

At the switching moment, the resonant tank resonates with parasitcal capacitance of primate switches $S_1 - S_4$ and damping resistance R_d . The equivalent circuit is an RLC series resonant circuit. To suppress the oscillations, the circuit is desired to work in the overdamped mode. Then, the damping resistance is designed as

$$R_d > 2\sqrt{\frac{L_r}{C'_p}} \quad (6)$$

where $C'_p = \frac{C_p C_r}{C_p + C_r}$.

Due to the small parasitic capacitance and large damping resistances, the oscillation can be quickly suppressed and i_r is quickly damped to zero by R_d . i_r is a decay of the transient current without oscillation and v_r could keep v_{r2} .

The operation in the negative half-switching cycle is similar to the positive one, which is not repeated here. According to the continuity and symmetry of v_r , we have

$$v_{r0} = V_i - 2nV_{bat} \quad (7)$$

$$v_{r1} = V_i \quad (8)$$

$$v_{r2} = -V_i + 2nV_{bat}. \quad (9)$$

With (1) and (4), the charging current can be calculated as

$$I_o = \frac{2}{T_s} \left(\int_0^{T_r/2} ni_r dt - \int_{T_r/2}^{T_r} ni_r dt \right) = \frac{2nV_i f_s}{\pi Z_r f_r}. \quad (10)$$

The charging current is independent of the output voltage achieving an inherent CC feature. Moreover, we can configure the charging current by choosing the switching frequency.

B. CV Operation Mode

When the battery voltage is charged high enough, the rectifier only conducts during $0 - T_r/2$ and the converter auto enters into the CV mode. The resonant current and voltage waveforms in this CV mode are illustrated in Fig. 2(b). There are three stages in a half-switching cycle in the CV mode.

1) *Stage 1* ($t_0 - T_r/2$): This stage is the same as Stage 1 in the CC mode. V_i charges V_{bat} through the resonant tank. i_r and v_r are identical to (1) and (2), which are not repeated here.

2) *Stage 2* ($T_r/2 - T_r$): S_2 and S_4 turn ON providing $v_{ab} = 0$. Unlike the CC mode, the rectifier diodes break in this stage due to the high battery voltage, as the circuit shown in Fig. 3(d). The resonant tank could resonate with the magnetic inductance. Since the magnetic inductance is far larger than the resonant inductance, the small magnetic current could slightly fall, which can be regarded as invariable and zero. The resonant voltage could maintain v_{r1} during this period.

3) *Stage 3* ($T_r - T_s/2$): Similar to Stage 3 in the CC mode, the transformer is shortened; thus, the magnetic current could fall to zero quickly. The resonant current and voltage keep zero and v_{r1} , respectively, at this stage.

The operation during the negative cycle is similar. Due to the continuity and symmetry of v_r , we have

$$v_{r0} = -v_{r1}. \quad (11)$$

According to (2), the output voltage is

$$nV_{\text{bat}} = V_i. \quad (12)$$

Moreover, the output current can be obtained as

$$I_o = \frac{2}{T_s} \int_0^{\frac{T_r}{2}} ni_r dt = \frac{-2nv_{r0}f_s}{\pi Z_r f_r}. \quad (13)$$

v_{r0} can be calculated based on the output current I_o . In other words, the resonant current and voltage are up to the output current. Large output current could lead to high resonant current and voltage.

C. Boundary Conditions

In the proposed control-free battery charger, the CC and CV operation modes are decided by the load conditions. To ensure that the converter works in the CC mode, the following three conditions should be satisfied:

$$V_i - v_{r0} \geq nV_{\text{bat}} \quad (14)$$

$$v_{r1} \geq nV_{\text{bat}} \quad (15)$$

$$|v_{r2}| \leq V_i. \quad (16)$$

To be specific, (14) makes D_1 and D_4 ON during Stage 1, (15) ensures that D_2 and D_3 are ON during Stage 2 to make the rectifier conduct during $0-T_r$, and (16) ensures that the primary switch antiparallel diodes can block the input voltage and make the resonant current discontinuous during $T_r-T_s/2$.

Using (7)–(16), the boundary condition between CC and CV modes can be achieved

$$V_i = nV_{\text{bat}}. \quad (17)$$

With the increase of load resistor, nV_{bat} could rise. Once V_{bat} reaches V_i/n , the rectifier could disconnect at stage 2; then, CC charging will not be maintained, and the converter automatically enters into the CV mode. According to (10) and (17), the critical load resistor $R_{L, \text{cri}}$ between CC and CV modes are

$$R_{L, \text{cri}} = \frac{\pi Z_r f_r}{2n^2 f_s}. \quad (18)$$

In the CC–CV charging method, first, the battery voltage is low, and a large current is needed to accelerate the charging speed. The load resistor could be very small, and the converter works in the CC mode. The current is constant, while the voltage rises from 0 to nV_{bat} , i.e., the equal resistor rises from 0 to $R_{L, \text{cir}}$. Specifically, the charging current is proportional to the switching frequency, making it be flexibly set by choosing a suitable frequency. Therefore, both slow charging with 0.1 C and fast charging with 2 C can be realized by the proposed method.

Battery voltage could rise with the increase in battery SOC as well as the load resistor. When the load resistor is larger than $R_{L, \text{cri}}$, the proposed converter could automatically transfer to the CV mode. The voltage is constant, while the current falls

to 0, i.e., the equal resistor rises from $R_{L, \text{cir}}$ to infinity. The battery voltage is clamped to V_i/n given in (12), and the charging current falls as the load resistor rises. The battery maximum safe threshold value can be obtained by regulating the input voltage V_i .

With the increase of the load, the proposed converter can automatically enter CV mode without SOC detection and active control. In other words, the proposed control-free battery charger enables automatic CC-to-CV transition. During the operation, the switching frequency is fixed rather than variable. Given a switching frequency, the automatic CC-to-CV feature can be achieved without any active control. Nevertheless, the switching frequency can be configured to achieve different CC outputs.

III. DESIGN CONSIDERATION

To implement the CC-CV features, the resonant tank of the converter should be carefully designed according to the battery charging requirements, the maximum charging current $I_{o, \text{max}}$ in the CC mode, and the safe threshold voltage value $V_{\text{bat}, \text{max}}$ in the CV mode.

A. Resonant Tank

The design procedure of the resonant tank is given as follows.

- 1) *Step 1*: Choose the maximum charging current $I_{o, \text{max}}$ and input voltage V_i . Choose the maximum switching frequency $f_{s, \text{max}}$.
- 2) *Step 2*: Determine the resonant frequency f_r , which is

$$f_r \geq 2f_{s, \text{max}}. \quad (19)$$

- 3) *Step 3*: Calculate the characteristic impedance Z_r , which should satisfy

$$Z_r \leq \frac{2nV_i f_{s, \text{max}}}{\pi f_r I_{o, \text{max}}}. \quad (20)$$

- 4) *Step 4*: Design the resonant tank

$$L_r = \frac{Z_r}{2\pi f_r} \quad (21)$$

$$C_r = \frac{1}{2\pi f_r Z_r}. \quad (22)$$

B. Transformer

As shown in Fig. 1, the transformer voltage is equal to v_{cd} that decides the magnetic flux density B and magnetic current.

1) *CC Mode*: Transformer voltage v_{cd} decides the varying ratio of magnetic current i_m . When v_{cd} is clamped to V_{bat} , i_m could linearly rise for half-resonant cycle. Then, v_{cd} reverses to $-V_{\text{bat}}$, leading to linearly decrement of i_m . Finally, v_{cd} is shortened by the damping circuit, making i_m remain zero. According to the i_m waveform, B_m is given as

$$B_m = \frac{V_{\text{bat}, \text{max}}}{2f_r N_2 A_e}. \quad (23)$$

2) *CV Mode*: Similarly, i_m also linearly rises for the first half-cycle due to $v_{cd} = V_{\text{bat}}$. During the next half-resonant cycle, v_{cd} is clamped to $-v_{r1}/n$, the maximum value of which

is V_{bat} . In stage 3, i_m could quickly fall to zero due to the damping resistor and remain zero during the half-switching cycle. Therefore, B_m is the same as the one in the CC mode, which is given in (23).

Considering the worst conditions, the practical magnetic flux density B should be smaller than the maximum value. Thus, the minimum turn ratio is derived as

$$N_2 = \frac{V_i}{2f_r B_m n A_e} \quad (24)$$

where n is the transformer turn ratio decided by

$$n = \frac{V_i}{V_{\text{bat}, \text{max}}}. \quad (25)$$

It should be noticed that because the transformer is shortened during the variable period $T_r - T_s/2$, the transform design is decided by the resonant frequency not the minimum switching frequency. Thus, the transformer size and core loss are not large even for a small switching frequency.

IV. LOSS ANALYSIS

The power loss of the converter mainly consists of switcher loss and magnetic devices loss (inductor and transformer). The switcher loss can be divided into switching loss and conduction loss. And magnetic device losses include conduction loss and core loss. It is necessary to consider all four sources of loss to improve the converter efficiency.

A. Loss of Power Switches

1) *Switching Loss*: According to the analysis in Section II, all the switchers realize both ZCS ON and OFF. Only the turn-OFF loss caused by the parasitic capacitance should be calculated, which is

$$P_{\text{OFF}} = \frac{1}{2} p C_{\text{ds}} V_{\text{ds}}^2 f_s. \quad (26)$$

Note that fully ZCS not only means ZCS ON but also ZCS OFF, while typically only sole ZVS ON can be realized in conventional methods. Compared with the conventional modulation scheme with sole ZVS ON, fully ZCS ON and OFF help in achieving high efficiency for the following reasons.

- 1) First, the switching loss can be reduced. Commonly, conventional modulation only achieves ZVS ON, but suffers from hard switching OFF. The total switching loss is given by $\frac{1}{2} V_{\text{ds}} i_{\text{off}} t_{\text{off}} f_s$, where i_{off} is the instantaneous current value when switch turns OFF and t_{off} is the turn-OFF time. When i_{off} is large due to phase lag or heavy load, the hard switching OFF loss is significant. The proposed modulation realizes both ZCS ON and OFF simultaneously; the total switching loss is only $\frac{1}{2} C_{\text{ds}} V_{\text{ds}}^2 f_s$. The ZCS-ON loss is small due to small junction capacitance C_{ds} (usually picofarad level) and regardless of load conditions.
- 2) Second, the conduction loss can be reduced. Since the proposed modulation realizes fully ZCS ON and OFF (similar to sinusoidal modulation), the backflow power can be eliminated. The resonant current is in phase with the

terminal voltage, and the conduction loss is reduced. However, the conventional modulations that cannot eliminate backflow power will incur higher conduction loss. That is a major reason why the proposed modulation enables high efficiency throughout the whole load range, while the conventional modulations suffer from efficiency deviation in the light-load conditions.

- 3) Third, fully ZCS ON and OFF can be achieved over the whole load range. Commonly, the conventional modulations meet difficulties in maintaining ZVS ON over a wide output range, especially in light-load condition. In the proposed method, the fully ZCS ON and OFF are independent of the load conditions.

For the above reasons, fully ZCS ON and OFF is an important characteristic of the proposed modulation, and it helps in high efficiency throughout the whole load range.

2) *Conduction Loss*: The conduction loss of the switchers is up to the RMS value of resonant converter $I_{r, \text{RMS}}$, which is decided by

$$P_{\text{sw.,cond.}} = \frac{1}{2} I_{r, \text{RMS}}^2 r_{\text{sw.}} \quad (27)$$

According to (1) and (4), $I_{r, \text{RMS}}$ in the CC mode is given as

$$I_{r, \text{RMS}} = \frac{1}{Z_r} \sqrt{\frac{f_s}{2f_r} [(nV_{\text{bat}})^2 + (V_i - nV_{\text{bat}})^2]}. \quad (28)$$

The conduction loss in the CC mode is in proportion to f_s , similar to the output power. Thus, f_s has no effect on the efficiency.

Similarly, in the CV mode, $I_{r, \text{RMS}}$ can be calculated as

$$I_{r, \text{RMS}} = \frac{I_o \pi}{2n} \sqrt{\frac{f_r}{2f_s}}. \quad (29)$$

Large f_s leads to small conduction loss in the CV mode, providing higher efficiency.

B. Losses of Magnetic Devices

The transformer and the resonant inductor are the two magnetic devices in the converter, which have similar power loss. This subsection only analyzes the power loss of the transformer.

1) *Transformer Conduction Loss*: The conduction loss of the transformer is also decided by $I_{r, \text{RMS}}$, which has been illustrated above. The conduction loss can be calculated by

$$P_{\text{tr.,cond.}} = I_{r, \text{RMS}}^2 r_{\text{tr.}} \quad (30)$$

2) *Transformer Core Loss*: Commonly, the generalized Steinmetz equation can be used to accurately calculate the transformer core loss, which is given as

$$P_{\text{tr.,core}} = V_T \frac{1}{T_s} \int_0^{T_s} k_1 \left| \frac{dB}{dt} \right|^\alpha |B(t)|^{\beta-\alpha} dt. \quad (31)$$

The coefficient k_1 is given by

$$k_1 = \frac{k}{(2\pi)^{\alpha-1} \int_0^{2\pi} |\cos \theta|^\alpha |\sin \theta|^{\beta-\alpha} d\theta}. \quad (32)$$

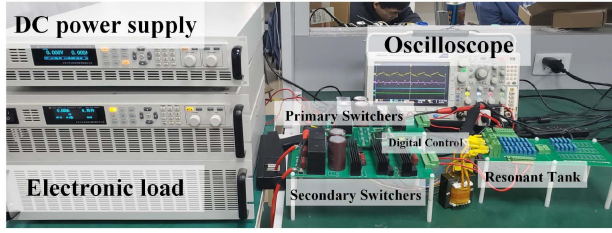


Fig. 4. Experimental setup.

The transformer core loss only occurs when magnetic flux density B varies.

As illustrated in Section II, during $T_r/2 - T_s/2$, switchers S_{s1} and S_{s2} are ON shortening the transformer. The transformer's B could be constant providing no core loss during this period. The core loss of the converter can be rewritten as

$$P_{tr,core} = V_T k \left(\frac{f_r}{2} \right)^{\alpha-1} B_m^\beta f_s. \quad (33)$$

B_m is calculated by (23), which is decided by the high resonant frequency f_r . Compared to the traditional methods, where core loss is up to the minimum switching frequency, a smaller core loss can be obtained by the proposed modulation. Moreover, the transformer core loss is linearly proportional to f_s , similar to the output power in the CC mode. f_s has no effect on the efficiency.

In conclusion, high efficiency was achieved for the following reasons.

- 1) The switching loss is small. Both ZCS ON and OFF are simultaneously realized over a wide output range in the proposed method; the total switching loss is independent of the load conditions, which is only 1 W in this article.
- 2) The conduction loss is small. A zero phase angle between the input voltage and current is obtained during the whole charging process in the proposed method, whereas large backflow current is needed in the conventional method, which results into large conduction loss.
- 3) The magnetic core loss is small. Commonly, large switching frequency could lead to large magnetic core loss. In the conventional method, the switching frequency varies with the load and is larger than the resonant frequency, whereas the switching frequency is fixed in the article and is only a quarter of the resonant frequency. Thus, the magnetic core loss is significantly reduced.

High efficiency can be achieved during the whole CC–CV charging process.

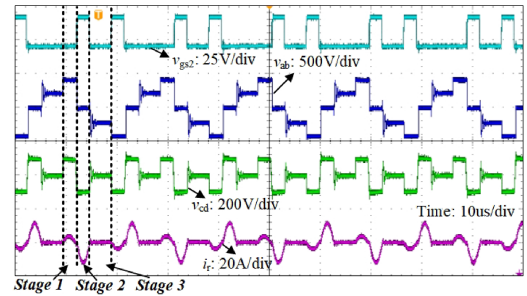
V. EXPERIMENTAL VERIFICATION

A 1-kVA experimental prototype of the SRC is built with specifications and parameters given in Table I. The experimental setup is shown in Fig. 4. An electronic load is used to emulate the practical battery. Both constant resistance (CR) and CV modes are used depending on the testing purposes. In the experiment, the SRC works in the CC mode ($i_o = 2.5$ A) and the CV mode ($V_{bat} = 420$ V).

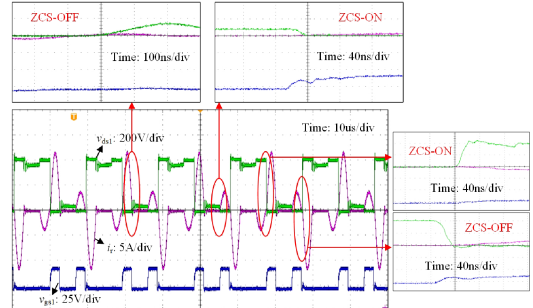
TABLE I
SPECIFICATIONS AND PARAMETERS OF THE SRC

Specifications		Symbols	Values
Primary side	Voltage range	V_i	400 V
	Current range	i_{in}	0–2.5 A
Secondary side	Voltage range	V_{bat}	0–420 V
	Current range	i_o	0–2.5 A

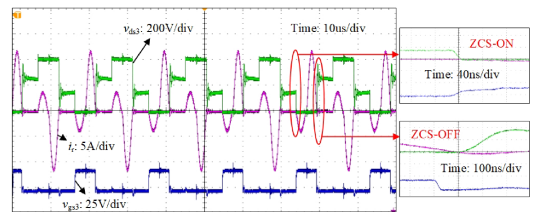
Parameters	Symbols	Values
Primary-side switches	$S_1 - S_4$	C3M0065090D
Secondary-side diodes	$D_1 - D_4$	NXPLQSC30650W6Q
Damping-circuit switches	$S_{s1} - S_{s2}$	C3M0065090D
Resonant inductor	L_r	20 μ H
Magnetic inductance	L_m	3.02 mH
Resonant capacitor	C_r	32 nF
Damping resistor	R_d	50 Ω
Resonant frequency	f_r	200 kHz
Turn ratio	n	18:19
Switching frequency	f_s	0–100 kHz



(a)



(b)



(c)

Fig. 5. Operation waveforms of the SRC for the CC mode. (a) Terminal voltage and resonant current waveforms. (b) Soft-switching waveforms of S_1 . (c) Soft-switching waveforms of S_3 .

A. Operating Waveforms

The operating and soft switching waveforms are captured in Figs. 5 and 6 depicting the CC and CV modes, respectively.

In the CC mode, the input voltage is $V_i = 400$ V, and the output current is $i_o = 2.5$ A. The electronic load works in the

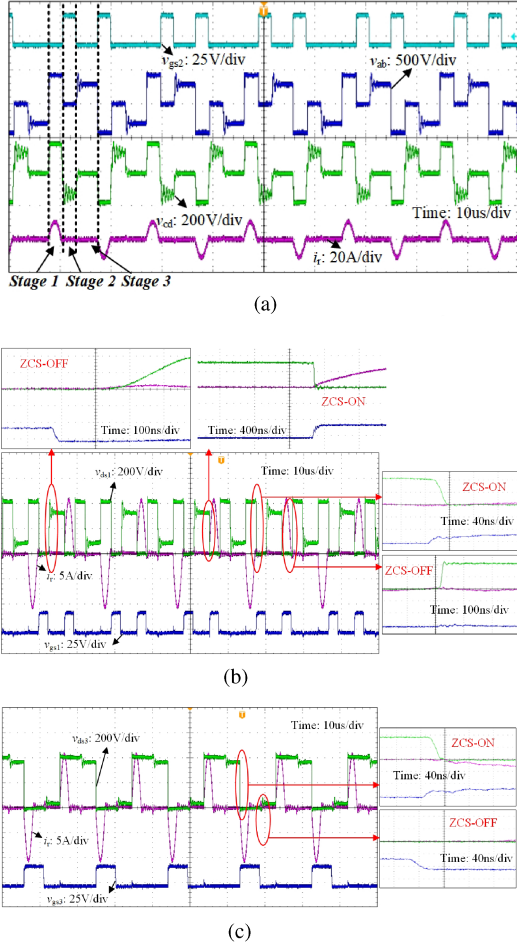


Fig. 6. Operation waveforms of the SRC for the CV mode. (a) Terminal voltage and resonant current waveforms. (b) Soft switching waveforms of S_1 . (c) Soft switching waveforms of S_3 .

CR mode, and the resistance is $R_L = 40 \Omega$. The output voltage is $V_{bat} = 100 \text{ V}$ and $f_s = 52 \text{ kHz}$. v_{ab} , v_{cd} , and i_r are consistent with the operating principle for the CC operating mode analyzed in Section II-B, as shown in Fig. 5(a).

In Stage 1, v_{ab} and v_{cd} are both high level; in Stage 2, v_{ab} is zero level and v_{cd} is negative level; in Stage 3, v_{ab} is resonating with C_p and R_d and quickly damped to zero, while v_{cd} is zero level. The waveform of i_r is sinusoidal and in phase with v_{ab} as well as v_{cd} ; therefore, there is no backflow power.

The soft switching waveforms of S_1 and S_3 are given in Fig. 5(b) and (c), while the switching waveforms of S_2 and S_4 are similar to S_1 and S_3 , which are not repeated here. The switches turn ON and OFF when the current is close to zero realizing ZCS ON and OFF simultaneously.

In the CV mode, $V_i = 400 \text{ V}$ and $V_{bat} = 420 \text{ V}$. The electronic load works in the CR mode and the resistance is $R_L = 266 \Omega$. Then, $i_o = 1.58 \text{ A}$ and $f_s = 52 \text{ kHz}$. v_{ab} , v_{cd} , and i_r are consistent with the operating principle for the CV operating mode analyzed in Section II-C, as shown in Fig. 6(a).

When v_{ab} and v_{cd} are both high levels for half the resonant period, then v_{ab} changes to zero for the next half-resonant period, while v_{cd} is resonating with magnetic inductance and

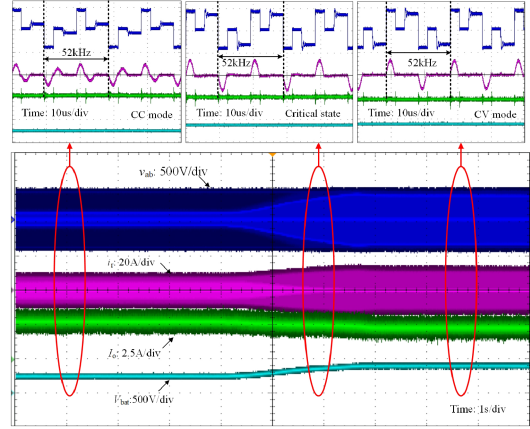


Fig. 7. Transition waveforms from CC to CV mode.

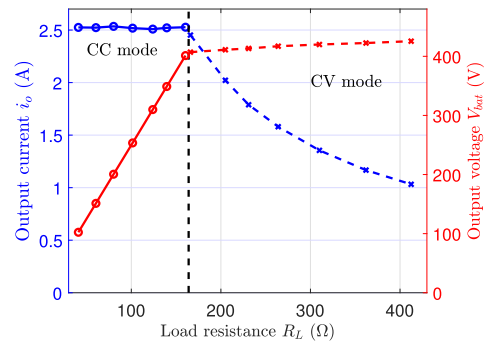


Fig. 8. Measured i_o and V_{bat} versus load resistance.

is negative level. For the rest time of the half-switching period, the waveforms of v_{ab} and v_{cd} are similar to the CC mode. The waveform of i_r slightly falls, which can be regarded as invariable during the second half of the resonant period; then, it is zero for the rest time of the half-switching period. Therefore, there is no backflow as well.

The soft switching waveforms of S_1 and S_3 are given in Fig. 6(b) and (c), while the switching waveforms of S_2 and S_4 are similar to S_1 and S_3 , respectively. All the switches turn ON and OFF when the current is close to zero realizing ZCS ON and OFF simultaneously.

Noticeably, in Fig. 6(a), the high ringing effect appears in stage 2, which is caused by the resonance between resonant tank, magnetic inductance, and transformer winding capacitance. Fortunately, the high ring can be clamped by the output voltage, and primary switches shorten the terminal voltage. The high ringing effect has no effect on the switches and input and output sides.

B. Transient Waveforms

Fig. 7 shows the transient waveforms from the CC mode to the CV mode. The SRC works without control during the whole transient conditions. The electronic load operates in the CV mode with a small resistance about 1Ω in series. The output voltage is changed from 250 to 418 V. The output current could fall from 2.5 to 2 A and the equal load resistance rises from 100 to 200 Ω .

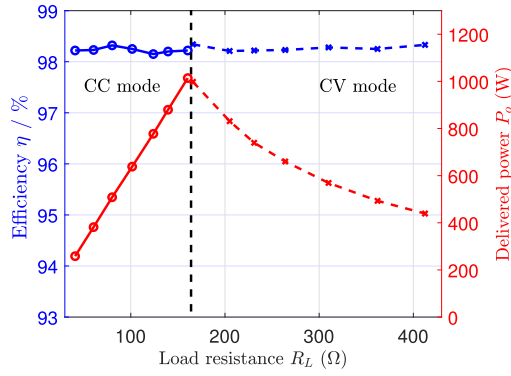


Fig. 9. Measured efficiency and power versus load resistance.

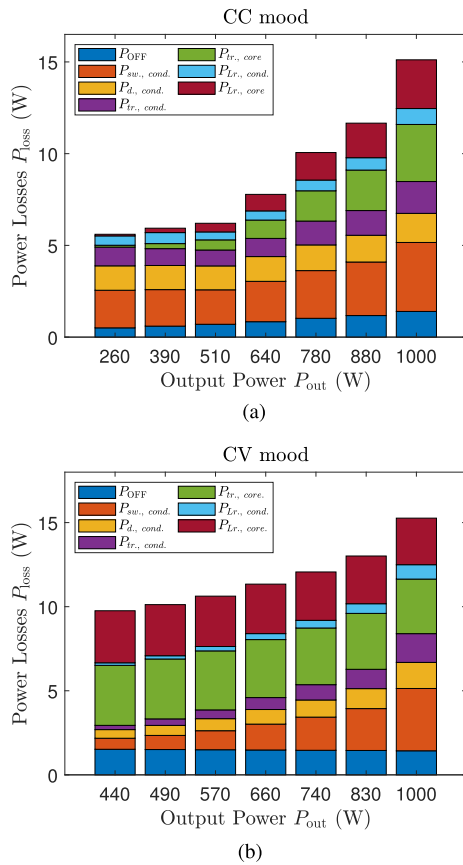


Fig. 10. Power loss breakdown for CC and CV modes. (a) Loss breakdown for $V_i = 400$ V and $i_o = 2.5$ A. (b) Loss breakdown for $V_i = 400$ V and $V_{bat} = 420$ V.

Auto transient from CC to CV mode can be obtained, which is perfectly suitable for the battery charging process.

C. Measured Output Characteristics

The measured output current i_o and voltage V_{bat} versus the equal load resistance is shown in Fig. 8. During the CC mode, i_o is maintained to 2.5 A with fixed $f_s = 52$ kHz, while V_{bat} rises with the increase of the load resistance R_L . When R_L is about 168 Ω , the converter enters into the CV mode. V_{bat} is

nearly invariable and slightly rises to 420 V with the decrease in i_o . Wide operating range and automatic CC-to-CV transition are achieved, obtaining control-free features.

D. Measured Efficiency

Measured efficiency and power versus load resistance are given in Fig. 9, where i_o is fixed to 2.5 A in the CC mode and V_{bat} is fixed to 420 V in the CV mode. The delivered power rises with the increase in V_{bat} in the CC mode and falls as i_o decreases during the CV mode, achieving the peak power 1000 W at the point of CC–CV.

It can be observed that the peak efficiency of the converter is nearly 98.4%, and the efficiency ranges from 98.1% and 98.4% during the whole CC and CV process. Fig. 10 also depicts the power loss breakdown. High efficiency can be achieved for the whole operating range, which perfectly adjusts the battery charging applications.

VI. CONCLUSION

To achieve CC and CV outputs for the battery charging applications, this article proposed a control-free battery charger based on the SRC. Wide voltage range from 0 to the rated value and wide load range from 0 to the rated power were acquired. Inherent f_s controlled current independent voltage and V_i controlled voltage independent current were obtained realizing accurate and control-free CC and CV outputs. Automatic and smooth CC-to-CV transition was also achieved by tackling the overcharging risk. Moreover, fully soft switching was realized for all the switches during the whole operating range, achieving high efficiency up to 98.4%. Experiment results validated the analysis well.

REFERENCES

- [1] M. Jahnes, L. Zhou, M. Eull, W. Wang, and M. Preindl, "Design of a 22 kW transformerless EV charger with V2G capabilities and peak 99.5% efficiency," *IEEE Trans. Ind. Electron.*, vol. 70, no. 6, pp. 5862–5871, Jun. 2023.
- [2] M. Yilmaz and P. T. Krein, "Review of battery charger topologies charging power levels and infrastructure for plug-in electric and hybrid vehicles," *IEEE Trans. Power Electron.*, vol. 28, no. 5, pp. 2151–2169, May 2013.
- [3] Z. Fang, Z. Wei, Z. Huang, and F. Liu, "Onboard energy storage system based on interleaved high-conversion-ratio quasi-resonant converter with small characteristic impedance," *IEEE Trans. Veh. Technol.*, vol. 70, no. 5, pp. 4238–4251, May 2021.
- [4] F. Liu, X. Ruan, and Y. Jiang, "Resonant peak suppression approaches for improving the dynamic performance of DCX-LLC resonant converter based two-stage DC-DC converter," *IEEE Trans. Ind. Electron.*, vol. 70, no. 6, pp. 5685–5695, Jun. 2023.
- [5] F. Musavi, M. Craciun, D. S. Gautam, W. Eberle, and W. G. Dunford, "An LLC resonant DC-DC converter for wide output voltage range battery charging applications," *IEEE Trans. Power Electron.*, vol. 28, no. 12, pp. 5437–5445, Dec. 2013.
- [6] J. Deng, S. Li, S. Hu, C. C. Mi, and R. Ma, "Design methodology of LLC resonant converters for electric vehicle battery chargers," *IEEE Trans. Veh. Technol.*, vol. 63, no. 4, pp. 1581–1592, May 2014.
- [7] X. Fang, H. Hu, Z. J. Shen, and I. Batarseh, "Operation mode analysis and peak gain approximation of the LLC resonant converter," *IEEE Trans. Power Electron.*, vol. 27, no. 4, pp. 1985–1995, Apr. 2012.
- [8] Z. Fang, T. Cai, S. Duan, and C. Chen, "Optimal design methodology for LLC resonant converter in battery charging applications based on time-weighted average efficiency," *IEEE Trans. Power Electron.*, vol. 30, no. 10, pp. 5469–5483, Oct. 2015.

- [9] N. Shafiei, M. Ordonez, M. Craciun, C. Botting, and M. Edington, "Burst mode elimination in high-power LLC resonant battery charger for electric vehicles," *IEEE Trans. Power Electron.*, vol. 31, no. 2, pp. 1173–1188, Feb. 2016.
- [10] H. Zeng, N. Gonzalez-Santini, Y. Yu, S. Yang, and F. Peng, "Harmonic burst control strategy for full-bridge series resonant converter-based EV charging," *IEEE Trans. Power Electron.*, vol. 32, no. 5, pp. 4046–4073, May 2017.
- [11] B. C. Kim, K. B. Park, and G. W. Moon, "Asymmetric PWM control scheme during hold-up time for LLC resonant converter," *IEEE Trans. Ind. Electron.*, vol. 59, no. 7, pp. 2992–2997, Jul. 2012.
- [12] H. Wu, X. Zhan, and Y. Xing, "Interleaved LLC resonant converter with hybrid rectifier and variable-frequency plus phase-shift control for wide output voltage range applications," *IEEE Trans. Power Electron.*, vol. 32, no. 5, pp. 4246–4257, May 2017.
- [13] Z. Fang et al., "Energy feedback control of light-load voltage regulation for LLC resonant converter," *IEEE Trans. Power Electron.*, vol. 34, no. 5, pp. 4807–4819, May 2019.
- [14] K. W. Kim, H. S. Youn, J. I. Baek, Y. Jeong, and G. W. Moon, "Analysis on synchronous rectifier control to improve regulation capability of high-frequency LLC resonant converter," *IEEE Trans. Power Electron.*, vol. 33, no. 8, pp. 7252–7259, Aug. 2018.
- [15] Y. Gu, Z. Lue, L. Huang, Z. Qian, and G. Huang, "Three-level LLC series resonant DC/DC converter," *IEEE Trans. Power Electron.*, vol. 20, no. 4, pp. 781–789, Jul. 2005.
- [16] S. Zhao, A. Kempitiya, W. T. Chou, V. Palija, and C. Bonfiglio, "Variable DC-link voltage LLC resonant DC/DC converter with wide bandgap power devices," *IEEE Trans. Ind. Appl.*, vol. 58, no. 3, pp. 2965–2977, May/Jun. 2022.
- [17] B. Li, Q. Li, Fred C. Lee, Z. Liu, and Y. Yang, "A high-efficiency high-density wide-bandgap device-based bidirectional on-board charger," *IEEE J. Emerg. Sel. Topics Power Electron.*, vol. 6, no. 3, pp. 1627–1636, Sep. 2018.
- [18] F. C. Lee, Q. Li, and A. Nabih, "High frequency resonant converters: An overview on the magnetic design and control methods," *IEEE J. Emerg. Sel. Topics Power Electron.*, vol. 9, no. 1, pp. 11–23, Jul. 2020.
- [19] S. W. Kang and B. H. Cho, "Digitally implemented charge control for LLC resonant converters," *IEEE Trans. Power Electron.*, vol. 64, no. 8, pp. 6159–6168, Aug. 2017.
- [20] Z. Fang, J. Wang, S. Duan, K. Liu, and T. Cai, "Control of an LLC resonant converter using load feedback linearization," *IEEE Trans. Power Electron.*, vol. 33, no. 1, pp. 887–898, Jan. 2018.
- [21] A. Nabih, M. Ahmed, Q. Li, and F. C. Lee, "Transient control and soft start-up for 1 MHz LLC converter with wide input voltage range using simplified optimal trajectory control," *IEEE J. Emerg. Sel. Topics Power Electron.*, vol. 9, no. 1, pp. 24–37, Feb. 2021.
- [22] V. B. Vu, D. H. Tran, and W. Choi, "Implementation of the constant current and constant voltage charge of inductive power transfer systems with the double-sided LCC compensation topology for electric vehicle battery charging applications," *IEEE Trans. Power Electron.*, vol. 33, no. 9, pp. 7398–7410, Sep. 2018.
- [23] J. Lu, G. Zhu, D. Lin, Y. Zhang, J. Jiang, and C. C. Mi, "Unified load-independent ZPA analysis and design in CC and CV modes of higher order resonant circuits for WPT system," *IEEE Trans. Transp. Electrific.*, vol. 5, no. 4, pp. 977–987, Dec. 2019.
- [24] X. Qu, H. Han, S. C. Wong, C. K. Tse, and W. Chen, "Hybrid IPT topologies with constant current and constant voltage output for battery charging applications," *IEEE Trans. Power Electron.*, vol. 30, no. 11, pp. 6329–6337, Nov. 2015.
- [25] T. N. Gucin, M. Biberoglu, and B. Fincan, "Constant frequency operation of parallel resonant converter for constant-current constant-voltage battery charger applications," *J. Modern Power Syst. Clean Energy*, vol. 7, no. 1, pp. 186–199, 2019.
- [26] M. Borage, S. Tiwari, and S. Kotaiah, "Analysis and design of LCL-T resonant converter as a constant-current power supply," *IEEE Trans. Ind. Electron.*, vol. 52, no. 6, pp. 1547–1554, Dec. 2005.
- [27] M. Borage, S. Tiwari, and S. Kotaiah, "LCL-T resonant converter with clamp diodes: A novel constant-current power supply with inherent constant-voltage limit," *IEEE Trans. Ind. Electron.*, vol. 54, no. 2, pp. 741–746, Apr. 2007.
- [28] H. H. Vu and W. Choi, "A novel dual full-bridge LLC resonant converter for CC and CV charges of batteries for electric vehicles," *IEEE Trans. Ind. Electron.*, vol. 65, no. 3, pp. 2212–2225, Mar. 2018.



Zhijian Fang (Member, IEEE) received the B.S. and Ph.D. degrees in electrical engineering and automation from the Huazhong University of Science and Technology, Wuhan, China, in 2010 and 2015, respectively.

From 2015 to 2018, he was a Postdoctoral Research Fellow with the School of Electrical Engineering, Wuhan University, Wuhan. From February 2016 to January 2017, he was a Postdoctoral Research Fellow with the Department of Electrical and Computer Engineering, Ryerson University, Toronto, ON, Canada.

Since 2019, he has been a Professor with the School of Automatic, China University of Geosciences, Wuhan. His research interests include high performance dc–dc converters, battery chargers, and renewable energy applications.



Haojiang Yue (Student Member, IEEE) received the bachelor's degree in automation in 2020 from the China University of Geosciences, Wuhan, China, where he is currently working toward the master's degree in control engineering.

His research interests include dc–dc resonant converters.



Zihao Wei (Student Member, IEEE) received the bachelor's degree in electrical engineering and automation from the Harbin Institute of Technology, Harbin, China, in 2018. He is currently working toward the master's degree in automation engineering with the Department of control science and engineering, China University of Geosciences, Wuhan, China.

His research interests include dc–dc converters and their control method.



Zihan Zhang (Student Member, IEEE) received the bachelor's degree in electrical engineering from Yan-shan University, Qinhuangdao, China, in 2021. He is currently working toward the master's degree in automation engineering with the China University of Geosciences, Wuhan, China.

He is also with the School of Automation, China University of Geosciences. His research interests include power electronics and energy harvesting.



Zhicong Huang (Member, IEEE) received the B.Eng. degree in electrical engineering and automation and the M.Eng. degree in mechanical and electronic engineering from the Huazhong University of Science and Technology, Wuhan, China, in 2010 and 2013, respectively, and the Ph.D. degree in power electronics from the Hong Kong Polytechnic University, Hong Kong, in 2018.

He is currently an Associate Professor with the Shien-Ming Wu School of Intelligent Engineering, South China University of Technology, Guangzhou,

China. From January 2019 to February 2020, he was a Postdoctoral Fellow, under the UM Macao Talent Program, with the State Key Laboratory of Analog and Mixed-Signal VLSI, University of Macau, Macao, China. His research interests include wireless power transfer, power electronics penetrated power systems, electric vehicles, and intelligent engineering.

Dr. Huang received the Outstanding Reviewer Award from IEEE TRANSACTIONS ON POWER ELECTRONICS in 2021.